PAPER

The fabrication of Ti₃C₂ and Ti₃CN MXenes by electrochemical etching†

Kai Chio Chan,[a] Xiang Guan,[a] Teng Zhang,[c] Kailing Lin,[a] Yihe Huang, [b] Lingshu Lei,[a] Yiannis Georgantas,[a] Yury Gogotsi,*[c] Mark A. Bissett [*a] and Ian A. Kinloch [*a]

2D MXenes are well-known for their outstanding performance in electrochemical energy storage and many other applications owing to their high conductivity and specific surface area. An obstacle to the wider synthesis of MXenes for research and industrial applications is the use of hazardous hydrofluoric acid (HF) during their synthesis. Herein, we developed the electrochemical etching process for the synthesis of Ti₃C₂ and Ti₃CN MXenes by using aqueous tetrafluoroboric acid as the electrolyte, thus only involving a very low concentration of HF. The effect of electrical potential and temperature on the etching rate is studied and compared to chemical etching with HBF₄. A mechanism based on the selective anodic dissolution of aluminium from Ti₃AlC₂ and Ti₃AlCN with the tetrafluoroborate ion is proposed. The MXene formation was confirmed by Raman spectroscopy, X-ray photoelectron spectroscopy, X-ray diffraction and electron microscopy. The MXene flakes from the electrochemical etching process have larger lateral dimensions compared to chemically etched MXene flakes as a result of the suppression of the HF decomposition and rapid etching rate. The electrodes of lithium-ion supercapacitors made from electrochemically etched Ti₃C₂ and Ti₃CN exhibited cycle performance and rate capabilities comparable to HF-etched MXenes.

1. Introduction

MXenes, two-dimensional transition metal carbides, nitrides, and carbonitrides, have received a tremendous amount of research attention since its discovery in 2011.[1] The high specific surface area, hydrophilicity, conductivity, and mechanical strength of MXenes make them promising for applications including energy storage,[2–7] electromagnetic interference shielding,[8–10] and catalysis.[11] MXenes can be described as a hexagonal close packed structure with the composition $M_{n+1}X_nT_x$ ($n = 1$ to 4; where M is an early d block transition metal; X is carbon or nitrogen; T is surface terminatal groups such as $=O$, $–OH$, $–Cl$, and $–F$, depending on the chemical etchant).[12] Terminal group free MXenes ($M_{n+1}X_nT_0$) are determined to have D_{3d} symmetry.[13] However, the presence of the terminal groups distorts the symmetry of the unit cell. Hence, the literature generally refers to the unit cell of $M_{n+1}X_nT_0$ as pseudo-$P6_3/mmc$.[14]

MXenes are fabricated from corresponding MAX phases with the chemical composition of $M_{n+1}AX_n$, where A is either group 3 or 4 elements (*e.g.*, Al, Ga, Si) lying between the MXene layers.[15–18] MXenes have very diverse chemical compositions due to the different combinations of M, A, and X elements. To date, more than 50 MXenes have been reported to be successfully synthesised.[12] The family of MXenes is further expanded when two transition metals are mixed in an MXene structure, in which the transition metal atoms may either be arranged randomly across all the M layers, or they may form ordered structures.[19–21] Given that the ratio of M and X in these double transition metal MAX precursors can be controlled as needed, the number of possible MXenes can be limitless.

Conventionally, the synthesis of MXene requires the use of hydrofluoric acid, either on its own or mixed with other acids (*e.g.*, HCl, H₂SO₄),[1,17,18,22,23] or the use of reagents that release HF *in situ* (*e.g.*, LiF + HCl, known as the MILD approach, and NH₄HF₂) to remove the A layer from the MAX precursor.[24–26] However, HF is extremely hazardous to humans and the environment. Furthermore, the aggressiveness of HF causes unavoidable damage to the basal plane of the MXene layer, resulting in a small flake size of the delaminated MXenes. A few hydrothermal approaches have been reported to etch the MAX phase to MXene. Gentile *et al.* reported the hydrothermal etching of Ti₃C₂ using HBF₄ as an etchant.[27] Yet, the etching mechanism was still based on the decomposition of HBF₄ to HF upon heating to 60 °C. Another example, inspired by the Bayer process used in bauxite refining for the isolation of aluminium

ᵃAdvanced Nanomaterials Group, Henry Royce Institute, Department of Materials, The University of Manchester, Oxford Road, M13 9PL, UK. E-mail: mark.bissett@manchester.ac.uk; ian.kinloch@manchester.ac.uk

ᵇLaser Processing Research Centre, Department of Mechanical Aerospace Civil Engineering, University of Manchester, Oxford Road, M13 9PL, UK

ᶜA. J. Drexel Nanomaterials Institute and Department of Materials Science and Engineering, Drexel University, Philadelphia, PA 19104, USA. E-mail: gogotsi@drexel.edu

This journal is © The Royal Society of Chemistry 2024

J. Mater. Chem. A, 2024, **12**, 25165–25175 | 25165

oxide,[28] is a fluorine-free synthesis of $Ti_3C_2T_x$ via alkali treatment reported by Li et al., which involves the use of 27.5 M of NaOH at 270 °C for 12 hours.[29] Peng et al. reported a hydrothermal etching of MAX phases (Ti_3AlC_2 and Nb_2AlC) by 12 M HCl and 0.5 M $NaBF_4$ for up to 32 hours at 180 °C.[30] Alternatively, non-aqueous approaches such as molten salt and halogen etching have also been reported.[31–36] However, the abovementioned approaches require harsh reaction conditions, making them costly and difficult to scale up. They may also damage, oxidise or hydrolyse MXene nanosheets.

Amongst all other approaches, electrochemical etching of MAX phases is particularly promising. Electrochemical fabrication of 2D materials is well studied for graphene, 2D-MoS_2, and mono-elemental Xenes.[37,38] In van der Waals solids, upon applying electrical potential, the ion intercalation or gas evolution between the 2D material layers causes the interlayer spacing to expand, overcoming the van der Waals forces and ultimately exfoliating the bulk layered material into its 2D form. The major advantage of electrochemical exfoliation is its environmental friendliness. Using graphene as the example, electrochemical exfoliation involves milder chemicals as the electrolyte (e.g., Na_2SO_4 or other sulfate salts) in contrast to the Hummers' method (concentrated H_2SO_4 and H_3PO_4 in combination with $KMnO_4$).[39,40] Despite the success of electrochemical exfoliation in the synthesis of graphene and other 2D materials, there are very few reports on the electrochemical fabrication of MXenes. The main obstacle originates from the unique interlayer interaction of the MXene layer in the MAX phase precursor. Unlike other bulk laminated materials, the M–A–M chemical bonding between the MXene layers in the bulk MAX phase precursor is significantly stronger than the physical van der Waals force between the layers in graphite. Thus, the electrochemical exfoliation processes need to chemically selectively etch the A layer in addition to expanding the interlayer distance. Furthermore, unlike the carbon in the strong sp^2-hybridised framework in graphene, the transition metal in MXenes is prone to oxidize if the voltage applied is over its oxidation potential (c.f. for the anodic exfoliation of graphite, a voltage of up to +10 V can be applied).[39] Nonetheless, since the semi-covalent M–X bond is more thermodynamically stable than the weakly metallic M–A and A–A bonds, the selective oxidation of the A element is feasible under suitable conditions. The electrochemical etching of MAX phases has been reported using various types of HCl, NaCl, LiTFSI, and NH_4OH/NH_4Cl electrolytes.[41–46] However, the MXenes synthesised in those studies were mixed with carbide-derived carbon. This suggests that those electrolytes do not entirely remove the carbide generated during etching. Furthermore, the reaction setups reported in the literature are not scalable; working electrodes comprise MAX phases of ceramic pieces produced by cutting the ceramic or pressing the MAX phase powders into pellets.[43,45,46] However, the rate of the reaction would unavoidably be hindered by the limited surface area of the electrode. There are also reports of depositing MAX phase powders onto conductive material (e.g., carbon fiber clothes).[42,44] However, a binder is needed to ensure good contact. Furthermore, the use of CFC and the MXene p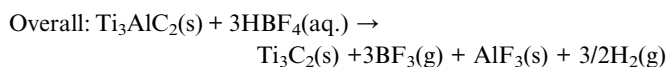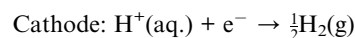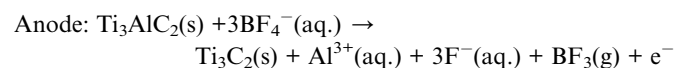roduced via this method is always mixed with the fiber residues caused by carbon fiber destruction during the washing process.

Herein, we report a low-HF synthesis of Ti_3C_2 and Ti_3CN MXenes via electrochemical etching, using HBF_4 as the electrolyte. The proposed mechanism allows the Ti_3AlC_2 and Ti_3AlCN precursors to undergo selective anodic dissolution of aluminium with the tetrafluoroborate ion. With the addition of the etching pathway provided by the presence of electrical potential, the etching of MXene is quicker and occurs at a lower temperature, minimising the release of HF. The role of electrical potential in accelerating the etching was studied. Furthermore, the influence of temperature for both electrochemical and chemical etching with HBF_4 was studied. As a result of the suppression of HF decomposition and etching time, the electrochemically etched MXene exhibits a larger lateral size compared to the MXene produced by chemically etching in HF or HBF_4. The energy storage performance of the electrochemically etched Ti_3C_2 and Ti_3CN in lithium-ion batteries is tested and mimics the superior cycle performance and rate capabilities of chemically etched MXene. The electrochemically etched Ti_3C_2 and Ti_3CN anodes exhibit superior cycle performance and rate reversibility for lithium-ion supercapacitors. For clarification, the electrochemically etched Ti_3C_2, Ti_3CN and MXene will be labeled EE-Ti_3C_2, EE-Ti_3CN, and EE-MXene, respectively. MXenes that are chemically etched by HBF_4 will be labeled CE-MXene. MXene etched by HF and HCl will be labeled HF/HCl-MXene.

2. Results and discussion

2.1 Mechanism

Fig. 1a schematically shows the setup of the reaction. A graphite crucible was used as the reaction container and the current collector for the MAX phase powder. This approach allowed the etching of the MAX phase in its powder form without using a binder, as all MAX phase particles settled at the bottom of the graphite crucible during the etching process. Pt wire was used as the cathode. However, it is worth mentioning that the etching can also be carried out with graphite as the counter electrode, which suggests that the hydrogen evolution does not have to occur on the surface of platinum. For the electrochemical etching, the mechanism was proposed as follows:

$$\text{Anode: } Ti_3AlC_2(s) + 3BF_4^-(aq.) \rightarrow$$
$$Ti_3C_2(s) + Al^{3+}(aq.) + 3F^-(aq.) + BF_3(g) + e^-$$

$$\text{Cathode: } H^+(aq.) + e^- \rightarrow \tfrac{1}{2}H_2(g)$$

$$\text{Overall: } Ti_3AlC_2(s) + 3HBF_4(aq.) \rightarrow$$
$$Ti_3C_2(s) + 3BF_3(g) + AlF_3(s) + 3/2H_2(g)$$

The anodic polarisation of the MAX phase triggers the dissolution of aluminium accompanied by the release of BF_3 gas, whilst a proton is reduced to hydrogen gas on the surface of the cathode. Note that +1 V was applied to all electrochemical etching to minimize the oxidation of the MXene. The initial concentration of HBF_4 in both electrochemical and chemical etching was 24%.
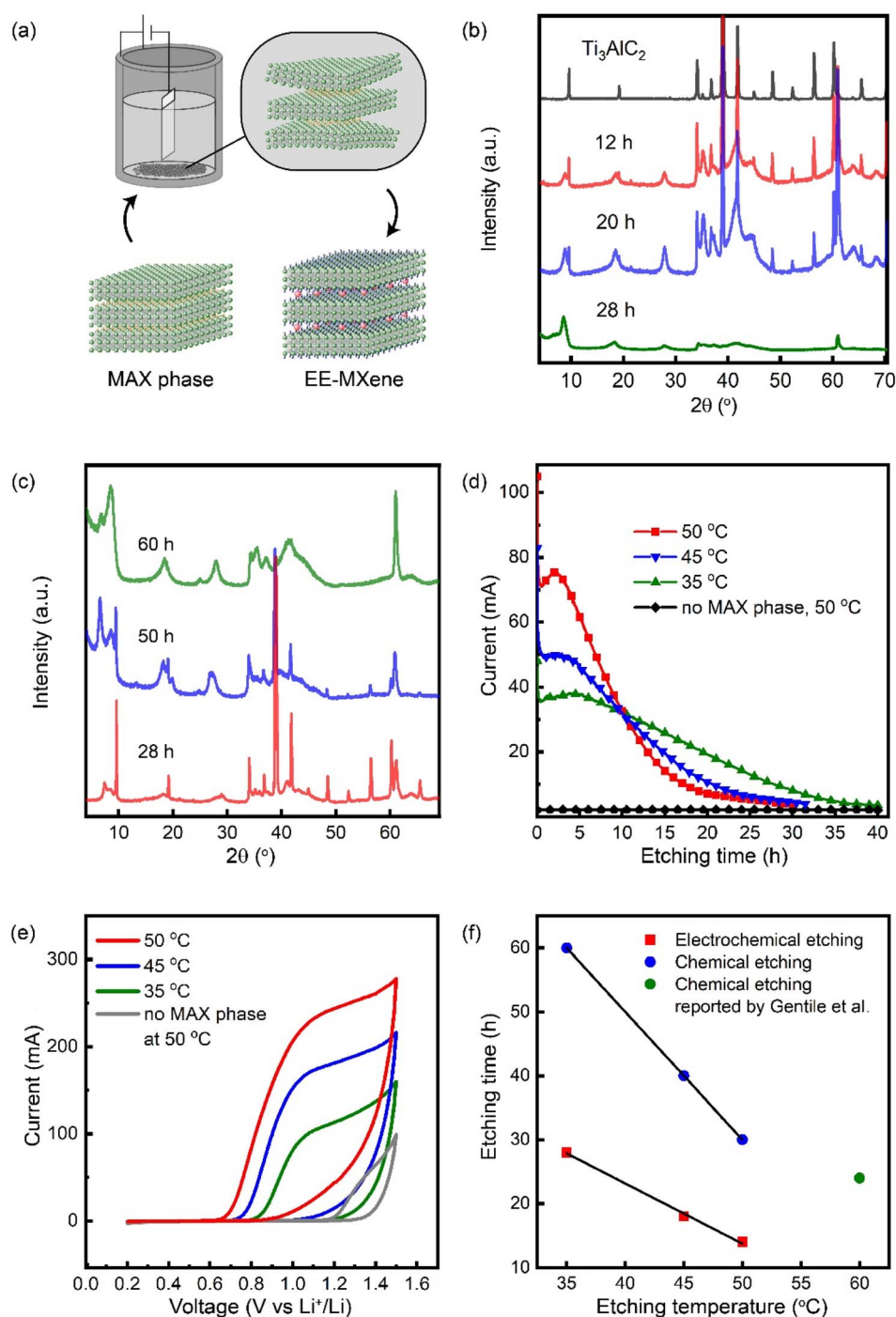
25166 | J. Mater. Chem. A, 2024, **12**, 25165–25175

This journal is © The Royal Society of Chemistry 2024

Fig. 1 (a) Schematic illustration of the setup. (b) XRD of EE-Ti_3C_2 etched with an applied voltage of +1 V at 35 °C with different etching times. (c) XRD pattern of CE-Ti_3C_2 at 35 °C with different etching times. (d) Amperometric monitoring of the electrochemical etching of EE-Ti_3C_2 at various temperatures. (e) Cyclic voltammetry curve of 1 g of Ti_3AlC_2 at various temperatures. Scan rate: 10 mV s^{-1}. (f) Etching time required to completely etch Ti_3AlC_2 to Ti_3C_2 by electrochemical etching and electrochemical etching at various temperatures.

2.2 XRD analysis

Fig. 1b gives the XRD pattern of the electrochemically etched Ti_3C_2 and shows the change of the crystal lattice upon etching the MAX phases to give MXene. Upon electrochemically etching with HBF_4 for 28 hours at 35 °C, the (002) peak of the Ti_3AlC_2 precursor at 9.52° was shifted to 8.63°. According to Bragg's law

and the reciprocal-space metric tensor equation of hexagonal crystal lattices, this corresponds to a change of d-spacing from 9.31 Å to 10.26 Å, equivalent to a change of c-LP from 18.62 Å to 20.52 Å. The increased interlayer spacing was also accompanied by an increase of FWHM from 0.10 to approximately 0.6, which is attributed to the decrease of crystallinity upon the removal of

This journal is © The Royal Society of Chemistry 2024

J. Mater. Chem. A, 2024, **12**, 25165–25175 | **25167**

aluminium which allows the introduction of surface termination and water intercalant. Peaks observed between 30 and 50° correspond to carbide and intermetallic impurities derived from the MAX phase precursor. After electrochemical etching, these peaks are no longer observable, indicating the effective removal of these impurities. Instead, a broad peak was observed, corresponding to the higher-order peaks of the multilayer MXene.[47] The XRD showing similar behavior for EE-Ti₃CN can be found in Fig. S1.† Whilst electrochemical etching at 35 °C only required 28 hours for the 100% conversion from MAX phases to MXene, the time required for the complete etching with HBF₄ in the absence of voltage at 35 °C was 60 hours (Fig. 1c). Note that for some MXene samples, two (002) peaks were observed due to the different amounts of water and ions intercalated between the MXene layers.[48]

Fig. 1d shows the amperometry of electrochemical etching carried out at 35 °C, 45 °C, and 50 °C, respectively. In general, a correlation between the aluminium content in the MAX phases with the etching current can be seen. Initially, a high current is always observed; this is due to the anodic dissolution of aluminium oxide impurities mixed with the MAX phase precursor. After that, the current becomes stable and gradually decreases as the etching time increases. This is because of the decrease of aluminium content in the MAX phases as etching time increases. Furthermore, the drop in etching current may be attributed to the fact that the anodic dissolution of the aluminium closer to the surface occurs at a faster rate than the aluminium in the core of the crystal. When the etching is completed, the current will soon reach a plateau, as all the aluminium in the MAX phase is consumed by the anodic dissolution. At this stage, the current flow detected is mainly contributed to the introduction of surface terminations, as a higher amount of O and F content is detected for over-etched MXene (further discussed in the XPS section). The presence of this current plateau is also an indication that both Ti₃C₂ and Ti₃CN are stable and have a slow oxidation rate under the applied conditions. The time required for the electrochemical etching at various temperatures to reach the stable plateaus coincided with the time required to completely diminish the MAX precursor peaks at that temperature as per the XRD analysis, making it particularly useful for monitoring the etching process. Furthermore, it is worth mentioning that when no MAX phase is present in the graphite crucible, no current flow is observed. This further confirmed the proposed mechanism that the redox reaction occurs at the MAX phase surface, resolving the debate that the electrochemical etching is triggered by the electrochemical decomposition of HBF₄ to HF.

Upon integration of the current flow throughout the electrochemical etching process, each Ti₃AlC₂ crystal unit consumes 4.5 electrons (4.7 electrons for Ti₃AlCN) when it is etched for 28 h at an etching temperature of 35 °C (calculation in the ESI†). The value is expected to be slightly overestimated as part of the current flow may originate from the water electrolysis on the surface of the incompletely etched MXene. Yet, it concurs with the proposed mechanism that each aluminium requires 3 electrons for anodic dissolution, with the remaining 1.5 electrons contributing to the oxidation of the Ti₃C₂ surface.

2.3 Effect of voltage

Although the presence of an applied voltage facilitates the etching, controlling the magnitude is critical. Cyclic voltammetry was carried out to study the effect of voltage on the etching efficiency (Fig. 1e). At 35 °C, the rise of current occurs around +0.8 V, indicating that this is the minimum voltage for triggering the electrochemical etching at that temperature. The CV curve mimics a typical capacitor-like shape due to the electrical double layer formed on the surface of the semi-etched MAX phases. It is worth noting that the minimal voltage (V_{min}) required to trigger the electrochemical etching decreases as temperature increases (V_{min} at 45 °C = 0.7 V, V_{min} at 50 °C = 0.65 V). This coincides with the Nernst equation that reduction potential decreases as temperature increases. The fact that no current was detected in the control experiment when no MAX phase was present indicates that the flow of electrons is attributed to the redox reaction of the MAX phases with the electrolyte. Furthermore, it showed that HBF₄ does not undergo other side reactions under the etching voltage. Nevertheless, the increase of voltage beyond +1 V would, in fact, decrease the etching efficiency, despite an increase of current being observed. This is because when the voltage applied exceeds +1 V, the current detected is no longer solely associated with the anodic dissolution of aluminium of the MAX phases but also from the water electrolysis. Also, vigorous gas evolution may disturb the MAX phases from settling at the bottom of the crucible and thus terminating the etching. Therefore, despite water splitting playing an important role in facilitating the electrochemical exfoliation of other 2D materials, such as graphene and MoS₂, the vigorous evolution of gas on the surface of MAX phases only causes an isolation of the MAX phase surface from the electrode and the electrolyte.

2.4 Effect of temperature on etching

The time taken to remove the original (002) peak by electrochemical etching (t_{EE}) and chemical etching (t_{CE}) with HBF₄ at temperatures between 35 and 50 °C was measured using the diminishing intensity of the (002) of the MAX phase (Fig. 1f). It was found that both t_{EE} and t_{CE} decreased with increasing temperature. Yet, the effect of temperature was approximately twice as high for chemical etching time than for electrochemical etching. For instance, at 35 °C, t_{EE} and t_{CE} were observed to be 28 h and 60 h, respectively. By increasing the etching temperature to 50 °C, t_{EE} and t_{CE} reduce to 14 h and 30 h, respectively. Note that the etching time for chemical etching with HBF₄ at 60 °C reported by Gentile et al. is only present as a reference and was not counted in the fitting.[27] This difference in temperature dependence may be explained by the different etching mechanisms; the chemical etching with HBF₄ relies solely on the decomposition of HBF₄ to generate HF and the thermal energy to overcome the activation barrier in order to achieve the etching, whereas for the electrochemical etching with HBF₄, the presence of voltage provides an additional driving force by increasing the Fermi potential of the aluminium in the MAX phase precursor, allowing the anodic dissolution of aluminium to occur without the generation of

25168 | J. Mater. Chem. A, 2024, 12, 25165–25175

This journal is © The Royal Society of Chemistry 2024

HF. Compared to solely chemical etching with HBF_4, the extra reaction pathway provided by the electrochemical etching is concluded to be the main reason for the increased efficiency of etching at low temperatures. In addition, the electrolyte residue after electrochemical etching was dried by heating in a PTFE beaker. A white precipitate was formed after all the HBF_4 residue was evaporated. The FTIR spectrum of the white precipitate corresponded to aluminium oxide, further confirming the anodic dissolution of aluminium during the etching (Fig. S2†).

Fig. 2a shows the Raman spectra of the EE-Ti_3C_2 and EE-Ti_3CN and their MAX phase precursors. For EE-Ti_3C_2 that has undergone completed etching, peaks at 202 and 661 cm^{-1} originating from the A_{1g} (Ti, Al, C, O, F) and C (A_{1g}) modes of Ti_3AlC_2 MAX phases are no longer observable. Conversely, new peaks were detected at 210 and 727 cm^{-1} corresponding to the A_{1g} (Ti, C, O, F) and C (A_{1g}) modes of EE-Ti_3C_2. A broad peak was detected from 230 to 470 and 580 to 730 cm^{-1}, the literature attributes the region of this peak to the in-plane vibration of the terminal group on the MXene surface.[13] The peak at around 123 cm^{-1} is the resonant peak which is only detected when an excitation wavelength of 785 nm is used. For EE-Ti_3CN, the A_{1g} (C, N) peak appeared at 714 cm^{-1}. However, the A_{1g} (Ti, C, N, O, F) and A_{1g} (Ti, C, Al, N) peaks were not observed. This might be attributed to the peak broadening induced by the random arrangement of carbon and nitrogen atoms in the X plane. No peak was observed in the carbon region, suggesting that the EE-MXene is free from carbide-derived carbon.

X-ray photoelectron spectroscopy was performed to probe the composition and the oxidation state of the element. The wide scan of the EE-MXene can be found in Fig. 2b. High-resolution core-level scans were performed to get an insight into the oxidation state of each element. Upon successful etching, no Al_{2p} signal was detected for the EE-MXene. In terms of the termination group introduced during the etching, both fluorine and oxygen were detected. No boron was detected in all the etched samples, indicating that no Ti–O–BF_3 terminal groups were introduced. EE-MXene has a higher binding energy for the Ti 2p signal compared to its MAX phase precursor, as the aluminium in the MAX phases is substituted by O and F atoms,
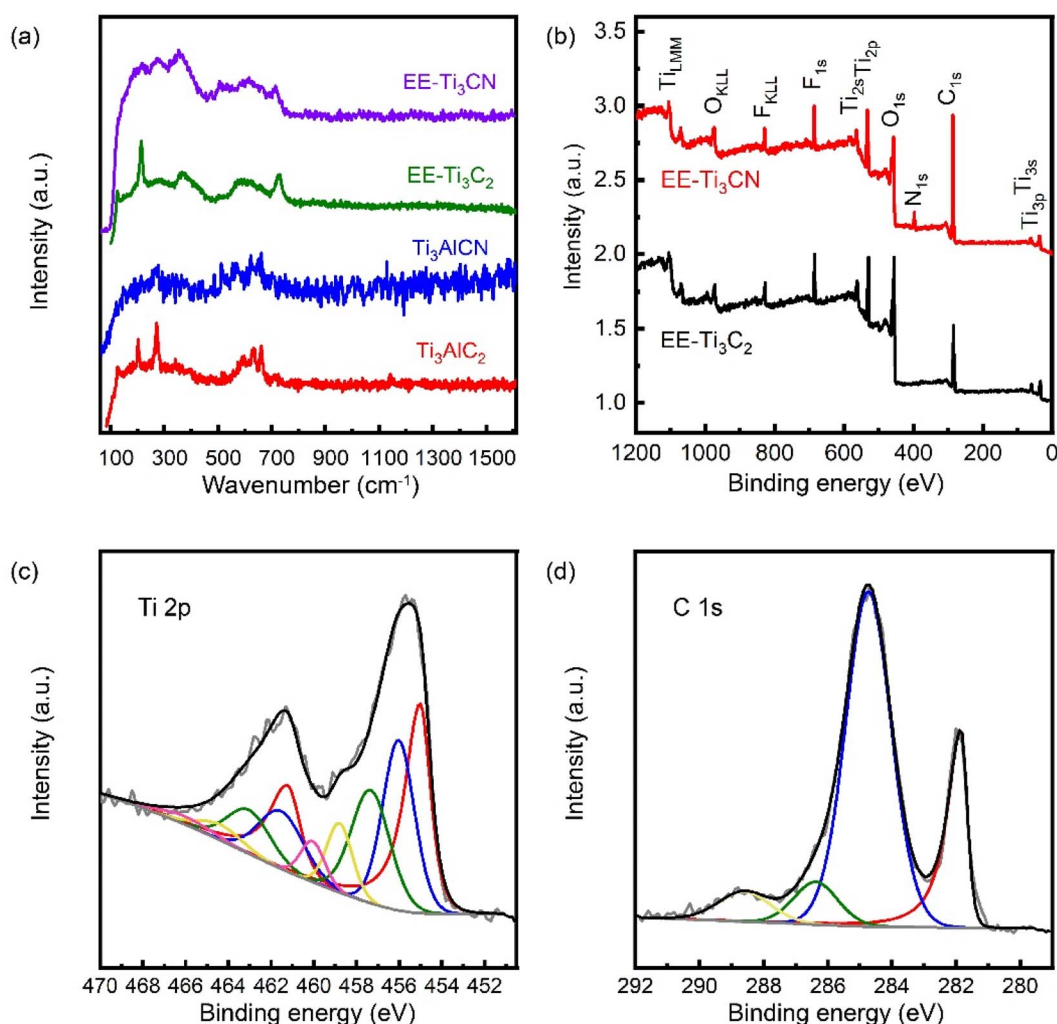

Fig. 2 (a) Raman spectrum of the EE-Ti_3C_2, EE-Ti_3CN, Ti_3AlC_2, and Ti_3AlCN. Excitation wavelength: 785 nm. (b) XPS survey spectrum of EE-Ti_3C_2 and EE-Ti_3CN. (c) XPS Ti 2p spectrum of EE-Ti_3C_2. (d) XPS C 1s spectrum of EE-Ti_3C_2.

This journal is © The Royal Society of Chemistry 2024

J. Mater. Chem. A, 2024, **12**, 25165–25175 | **25169**

Table 1 Stoichiometry of Ti_3C_2 and Ti_3CN etched by electrochemical etching of HBF_4, chemical etching of HBF_4, and chemical etching with HF and HCl

Sample	Etching conditions	Ti	C	N	O	OH	F	Cl
EE-Ti_3C_2	+1 V, 35 °C, 28 h	3	2		0.3	0.8	0.5	
EE-Ti_3C_2	+1 V, 35 °C, 36 h	3	2		0.3	1.1	1	
CE-Ti_3C_2	35 °C, 60 h	3	2		0.4	0.6	0.6	
HF/HCl-Ti_3C_2	35 °C, 24 h	3	2		0.2	0.3	0.6	0.2
EE-Ti_3CN	+1 V, 35 °C, 28 h	3	1.2	0.8	0.4	0.8	0.6	
HF/HCl-Ti_3CN	35 °C, 24 h	3	1.2	0.8	0.3	0.5	0.7	0.3

which are more electronegative. For the EE-Ti_3C_2, four pairs of doublets were assigned, corresponding to the titanium metal in the oxidation state of +1 to +3, and X–Ti–F of EE-Ti_3C_2, located at 454.6 (460.8), 455.7 (461.2), 457 (462.7), and 460.4 (466.4) (Fig. 2c). The remaining doublet located at 459.4 (465.4) was assigned to titanium oxide. For the C_{1s} spectrum (Fig. 2d), 4 singlets were assigned at 281.8, 284.7, 286.2, and 288.4 eV, corresponding to X–Ti, C–C, C–O, and C=O for EE-Ti_3C_2. For the N 1s signal of the EE-Ti_3CN, 4 peaks located at 396.4, 397.1, 399.5, and 402.4 eV are assigned for N–Ti, N–C, CH_3CN, and NH_4NO_3, respectively (Fig. S3†). Other core level scan results of EE-Ti_3CN can be found in Fig. S4 and S5.† A more detailed discussion of the X-ray spectroscopy of MXene can be found in the work by Halim et al.[49]

Table 1 lists the chemical composition of both the electrochemically and chemically etched MXenes. For comparison, MXenes chemically etched with the conventional mixed acid (HF and HCl) method were also evaluated. In general, the three different etching conditions led to a similar degree of fluoride termination. However, HF/HCl-MXene also had chloride termination, giving a higher content of halide termination overall. Both EE-Ti_3C_2 and CE-Ti_3C_2 exhibited a higher oxygen content than HF/HCl-MXene. No significant difference in chemical composition is observed for the CE-Ti_3C_2 and EE-Ti_3C_2 materials. This indicates that the acceleration of etching upon the application of voltage did not increase the oxidation of the EE-MXenes. This matches the current plateau observed from the amperometric monitoring during the electrochemical etching. Nevertheless, a significant increase in both oxygen and fluorine content was observed for the over-etched EE-Ti_3C_2. This shows that despite the electrochemical etching being more selective to the aluminium than the MXene, over-etching would still oxidise the MXene layer.

2.5 Morphology

Upon etching, the color of the EE-Ti_3C_2 multilayer powder changed from grey to dark grey for both EE-Ti_3C_2 and EE-Ti_3CN (Fig. S6†). When treated with TMAOH, the EE-Ti_3C_2 water dispersion appeared as a dark green solution. Fig. 3a shows the SEM images of EE-Ti_3C_2. Whilst resembling the laminated structure of the MAX phase precursor, EE-MXenes displayed an accordion-like structure due to the removal of the aluminium and the introduction of surface termination as well as water intercalation. Fig. 3b and c show the AFM images of

delaminated EE-Ti_3C_2 and the cross-sections of the flakes. The delaminated EE-Ti_3C_2 flake exhibited a smooth surface, and most of the flakes were observed to have a thickness of 3, 6, and 8 nm. Fig. 3d and e display the optical images of EE-Ti_3C_2 and its lateral size distribution of delaminated EE-Ti_3C_2 and HF/HCl-Ti_3C_2. For the delaminated HF/HCl-Ti_3C_2, most of the flakes had a lateral size of 2–3 μm. For EE-Ti_3C_2, flakes with lateral sizes as large as 9 μm are observable, indicating that the MXene basal plane was preserved during the etching. Nevertheless, it is worth noting that a significant reduction in the lateral size of the delaminated EE-Ti_3C_2 flake is observed for EE-MXenes, which are over-etched. The decrease of plane-to-edge ratio upon over-etching matched the increase of oxygen and fluoride content obtained from the XPS chemical composition. The ultrathin structure of the delaminated EE-Ti_3C_2 flake can also be observed in TEM (Fig. 3f), with a SAED pattern showing diffraction spots corresponding to the 110 (1.49 Å) and 100 (2.56 Å) planes of the hexagonal crystal lattice.[50] SEM and TEM images of EE-Ti_3CN can be found in Fig. S8 and S9.†

2.6 Li-ion supercapacitor

To study the intrinsic electrochemical properties of the EE-MXene, the energy storage performance of the EE-MXene was demonstrated and compared with that of the HF/HCl-MXene. The cyclic voltammetry curves of the half cell with EE-Ti_3C_2 and EE-Ti_3CN with lithium foil as a counter electrode are displayed in Fig. 4a. A reversible anodic peak at around +1 V was observed for all types of MXenes which is attributed to the Li ion insertion/extraction into/from the MXene layers. The peak current, I_{max}, of CV curves for both EE-Ti_3C_2 and EE-Ti_3CN increases as scan rates increase, with a relationship obeying the power law

$$I = av^b$$

with b, in the plot of $\log(i_{max})$ vs. $\log(v)$, being close to 1. This indicates that the charge storage mechanism is dominated by the capacitive effect.[51] Fig. 4c displays the galvanostatic charge/discharge profile of EE-Ti_3C_2 and EE-Ti_3CN at a current density of 0.1 A g^{-1}. The charge and discharge capacity for the first cycle was observed to have a coulombic efficiency of approximately 50%; this is attributed to the formation of a solid electrolyte interface upon the first charge and discharge cycle. Yet, the coulombic efficiency increases rapidly to 99.9% and stabilised after a few cycles, with a specific capacity of 175 mA h g^{-1} for EE-Ti_3C_2, 195 mA h g^{-1} for EE-Ti_3CN, 190 mA h g^{-1} for HF/HCl-Ti_3C_2 and 210 mA h g^{-1} for HF/HCl-Ti_3CN respectively. A tilted slope was observed during the charge and discharge process, indicating pseudocapacitance behavior. Fig. 4d and e show the cycle performance of all MXenes at a rate of 0.1 and 1 A g^{-1}, respectively. Before the charge/discharge at 1 A g^{-1}, pre-cycling was done at 0.1 A g^{-1} for 20 cycles as an activation process. For all MXenes, no capacity losses were observed at 0.1 A g^{-1} after 250 cycles at 0.1 A g^{-1}. In fact, an increase in capacity was observed and became more significant at a high current density. In general, all MXenes only reach their maximum capacity around a few decades of cycles. At 1 A g^{-1}, the peak capacity was
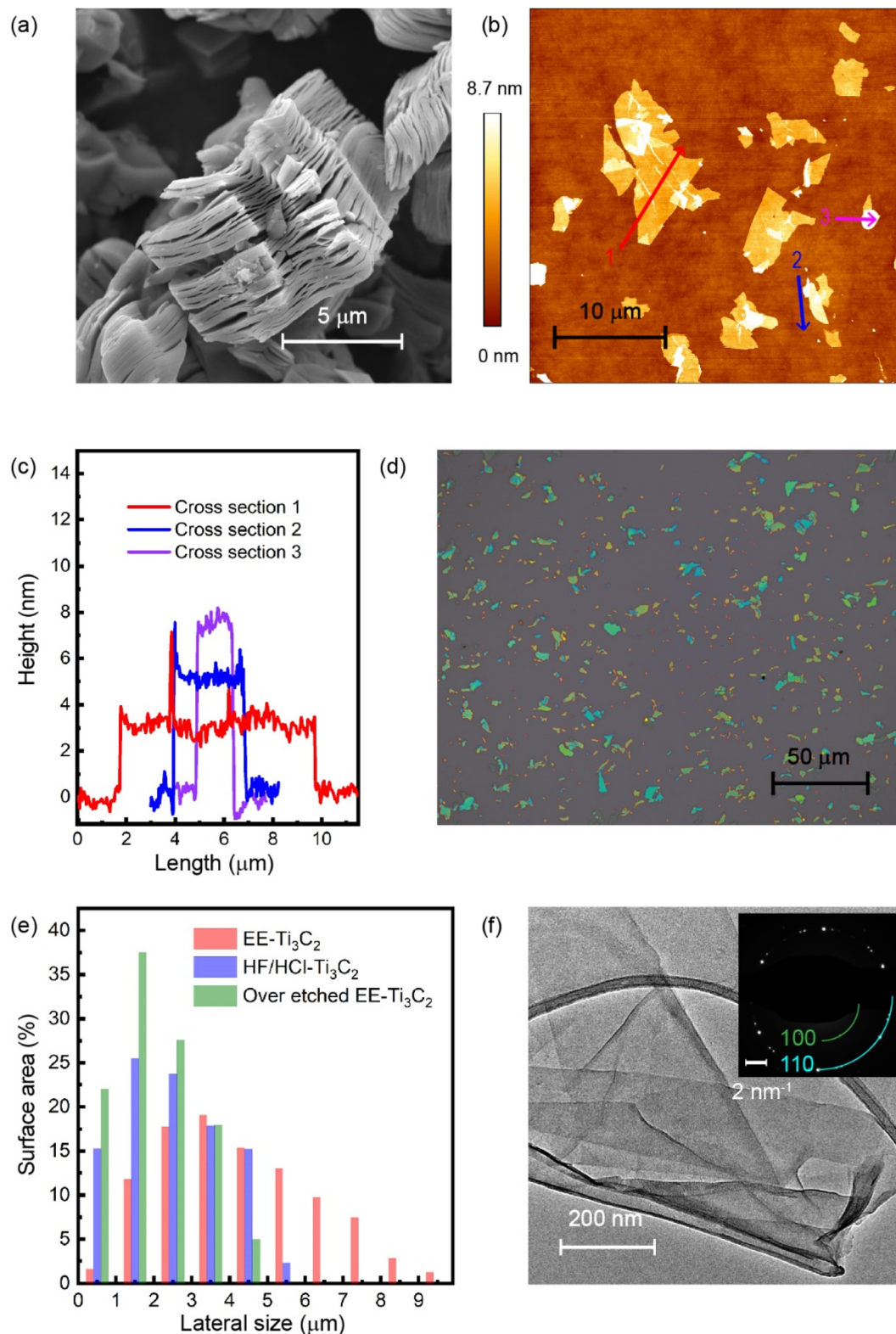
25170 | J. Mater. Chem. A, 2024, **12**, 25165–25175

This journal is © The Royal Society of Chemistry 2024

Fig. 3 (a) SEM image of EE–Ti$_3$C$_2$ multilayer powder. (b and c) AFM images and the cross-section of the delaminated EE–Ti$_3$C$_2$ flake. (d and e) Optical images of delaminated EE–Ti$_3$C$_2$. (d and e) Lateral size distribution of delaminated EE–Ti$_3$C$_2$ and HF/HCl–Ti$_3$C$_2$ flake. Overlapped flakes were excluded to avoid incorrect estimations. (f) TEM image of delaminated EE–Ti$_3$C$_2$ flake.

observed as follows: EE-Ti$_3$C$_2$ = 140 mA h g^{-1}, EE-Ti$_3$CN = 165 mA h g^{-1}, HF/HCl-Ti$_3$C$_2$ = 142 mA h g^{-1}, HF/HCl-Ti$_3$CN = 166 mA h g^{-1}. All MXenes exhibit superior cyclic performance, with a capacity retention of approximately 80% after 2000 cycles. The trend of increase in the capacity of MXene during cycling may be attributed to that of the irreversible expansion of
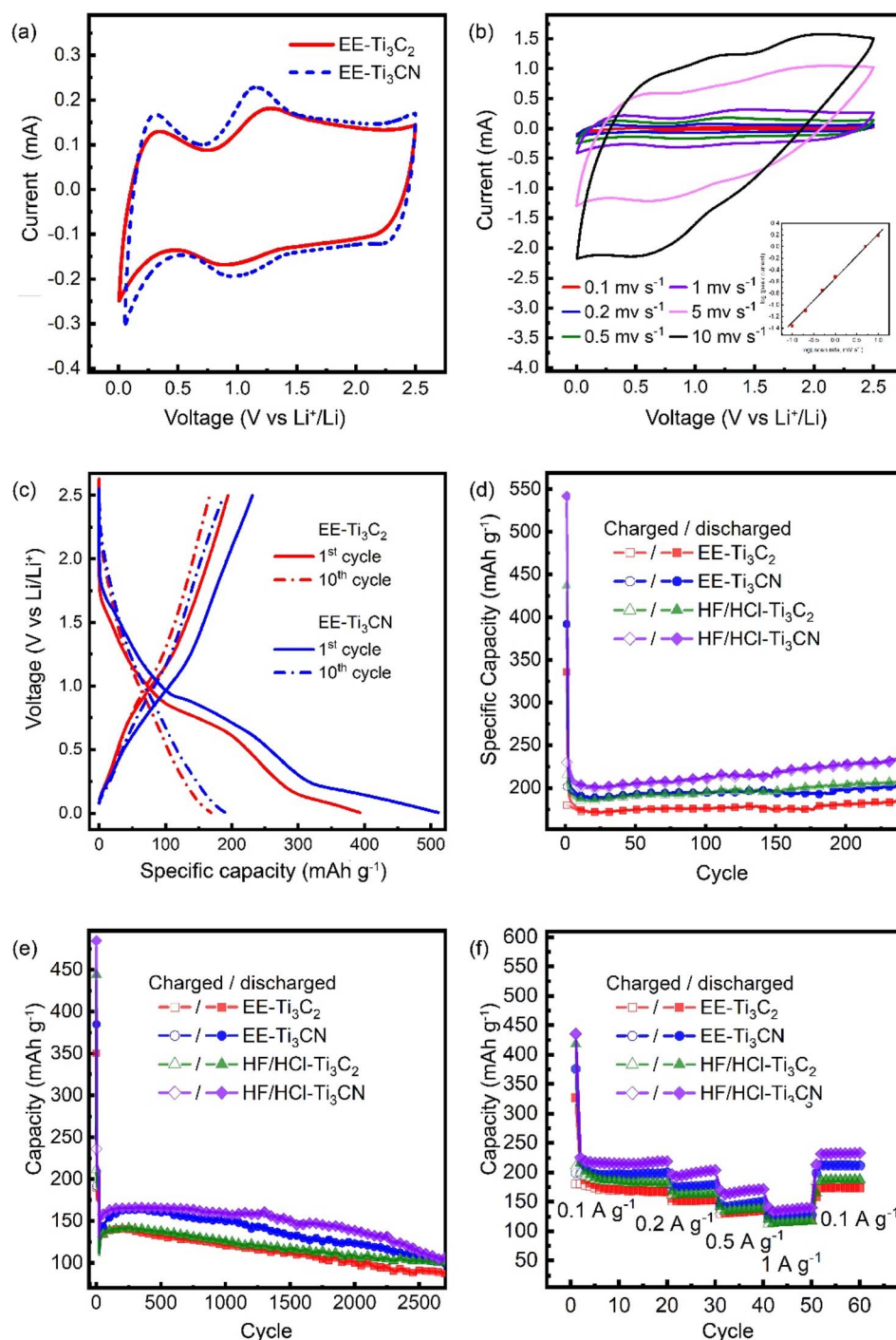
This journal is © The Royal Society of Chemistry 2024

J. Mater. Chem. A, 2024, **12**, 25165–25175 | **25171**

Fig. 4 (a) CV curves of EE-Ti$_3$C$_2$ and EE-Ti$_3$CN from 2.5 V to 0.05 V *vs.* Li/Li$^+$, obtained at a scan rate of 0.5 mV s^{-1}. (b) CV curves of EE-Ti$_3$C$_2$ at various scan rates. (c) Galvanostatic charge–discharge profiles of EE-Ti$_3$C$_2$ and EE-Ti$_3$CN at a current density of 0.1 A g^{-1}. (d) Cycle performance of EE-Ti$_3$C$_2$, EE-Ti$_3$CN, HF/HCl-Ti$_3$C$_2$, and HF/HCl-Ti$_3$CN at a current density of 0.1 and (e) 1 A g^{-1}. (f) Rate capability test of EE-Ti$_3$C$_2$ and EE-Ti$_3$CN and their HF/HCl etched analogs at 0.1, 0.2, 0.5, and 1 A g^{-1}.

the interlayer spacing caused by lithiation. Thus, more lithium can be accommodated between the MXene layers. This trend was also observed for other MXene energy storage systems.[31,52–54]

Both, EE-Ti$_3$C$_2$ and EE-Ti$_3$CN, showed slightly lower capacity than their HF/HCl etched analogues. Such difference is

attributed to the small amount of chloride termination in the HF/HCl-MXene, which is bulkier than the hydroxide and fluoride functional groups, creating wider spaces for the accumulation of lithium ions.[55] Furthermore, the differences in flake size are important; smaller flakes should increase the ionic conductivity (more pathways) while reducing the electronic

25172 | *J. Mater. Chem. A*, 2024, **12**, 25165–25175

This journal is © The Royal Society of Chemistry 2024

conductivity (higher ohmic resistance). The delaminated EE-MXene flakes showed a slightly larger lateral size in contrast to HF/HCl-MXene, making the latter more accessible to lithium deposition.[56] All MXenes exhibited good rate capability; the capacity decreased by approximately 60% when the rate increased from 0.1 to 1 A g^{-1}. The capacity was then recovered when the rate decreased back to 0.1 A g^{-1} without any loss of capacity, indicating good rate reversibility (Fig. 4d). The difference in capacity of all MXenes became smaller at high current capacity. This is because the current density is so high that the redox-active components were not able to undergo complete lithiation and delithiation. Therefore, at high current density, the redox contribution becomes less dominant and the electrode exhibits EDL-like behaviour, which is more dependent on the specific surface area.

3. Conclusions

This work has demonstrated that applying voltage can significantly increase the efficiency of the etching of MAX phases to produce MXene sheets with a large lateral size. The applied voltage allows the aluminium in both the Ti_3AlC_2 and Ti_3AlCN MAX phases precursor to undergo anodic dissolution. This extra reaction pathway significantly reduces the etching time and the etching temperature required for etching in HBF_4, and reduces the release of HF during the etching. Temperature accelerated both chemical and electrochemical etching but also may lead to over-etching and nanosheet damage. Compared to the conventional chemical approaches which use HF-based etchants, the electrochemical etching with HBF_4 is milder, faster, and safer to handle, with a high yield of 85%. Furthermore, unlike conventional HF approaches, in which temperature and concentration of the etchant are the only variables that control the reaction kinetics, voltage can provide further driving force to the reaction. This process may eventually be used to fabricate MXenes that cannot be etched by using HF. The simple experimental setup and mild reaction conditions of the electrochemical etching allow scale up for large-volume manufacturing. As the result of reduced etching time and HF exposure, the EE-MXene exhibits a bigger aspect ratio and less halide termination compared to HF-etched MXene. For energy storage applications, EE-MXene demonstrated the pseudocapacitive nature of energy storage in lithium-ion supercapacitors and exhibited superior cyclability and rate performance.

4. Experimental section

4.1 Electrochemical etching of MAX phases

MAX phase powder (1 g, 500 mesh, Nanoplexus) and HBF_4 (250 mL, 24% in H_2O) were added to a graphite crucible. A platinum wire was used as the counter electrode. The suspension was rested for 30 minutes until the electrolytes reached the desired temperature and all the MAX phase powders settled at the bottom of the crucible. +1 V was applied for 28 hours at 35 °C. After electrochemical etching, the MXene was washed with deionized water via vacuum filtration. The MXene was dried at 80 °C under vacuum for 15 hours. The dried EE-MXene was stored at 3 °C until further characterization application. The average yield of $EE-Ti_3C_2$ and $EE-Ti_3CN$ obtained was between 85% and 75%.

4.2 Chemical etching of MAX phases with HBF_4

The chemical etching with HBF_4 was carried out similar to the electrochemical etching, but without applying voltage.

4.3 Chemical etching of Ti_3AlC_2 with HF and HCl

The chemical etching of Ti_3AlC_2 with HF and HCl was carried out as reported elsewhere.[57] In brief, 1 g of Ti_3AlC_2 was slowly added to the chemical etchant and stirred at 300 rpm for 24 hours at 35 °C. The chemical etchant was a mixture of HF (48%, 2 mL) and HCl (37%, 12 mL), diluted with deionized water (volumetric ratio of $HCl : H_2O : HF = 6 : 3 : 1$). The resulting suspension was washed with deionized water several times via centrifugation until the pH of the suspension became neutral. The solid was collected via vacuum filtration and stored at 3 °C until further analysis.

4.4 Delamination

100 mg of EE-MXene was added to 10 mL of TMAOH (0.15 M) and stirred for 15 hours at 35 °C. The dispersion was washed with DI water until the pH of the dispersion became neutral. The suspension was sonicated for 1 hour to facilitate further delamination. The suspension was submerged in an ice bath with N_2 flow during the sonication to suppress the rate of oxidation. The dispersion was allowed to settle overnight at 3 °C, the supernatant was collected for further analysis.

4.5 Materials characterisation

Raman spectroscopy was carried out to study the vibrational mode of the MAX phase and MXene using an inVia confocal Raman microscope (Renishaw, Wotton-under-Edge, Gloucestershire, UK). X-ray diffraction patterns were obtained using a D8 autochanger (Bruker, Brighton, Sussex, UK) using Cu K_α radiation with a step size of 0.02° in the range of 3–90°. Atomic force microscopy was carried out to measure the thickness of the delaminated MXene flakes using a Nanowizard 4 XP Nanoscience atomic force microscope (Bruker, Brighton, Sussex, UK). SEM and TEM images were obtained to study the morphology using a Tescan Mira scanning electron microscope (Tescan, Kohoutovice, Czech Republic) and Talos transmission electron microscope (Thermofisher, Loughborough, UK), respectively. X-ray photoelectron microscopy was carried out to obtain the elemental composition and oxidation state of the MAX phase and MXene using an ESCA2SR spectrometer (ScientaOmicron GmbH) using monochromated Al K_α radiation (1486.6 eV, 20 mA emission at 300 W, 1 mm spot size) with a base vacuum pressure of $\sim 1 \times 10^{-9}$ mbar. Charge neutralisation was achieved using a low-energy electron flood source (FS40A, PreVac). Binding energy scale calibration was performed by defaulting the C–C in the C 1s photoelectron peak to be 284.7 eV. Analysis and curve fitting were performed using Voigt-approximation peaks using CasaXPS.

4.6 Electrochemical testing

The EE-MXene electrodes were prepared by mixing the MXene multilayer powders with super P carbon black, and polyvinylidene fluoride (PVDF) binder in N-methyl-2-pyrrolidinone (NMP) with a gravimetric ratio of 7 : 2 : 1 and the slurry was pasted on copper foil with a thickness of 100 μm and dried at 80 °C under vacuum overnight. A microporous membrane (Celgard 2400) was used as the separator. Cell assembling was carried out in an argon-filled glove box with the concentration of moisture and oxygen below 1 ppm. The electrolyte was 1 M $LiPF_6$ in ethylene carbonate and dimethyl carbonate in a 1 : 1 volumetric ratio. Galvanostatic charge–discharge tests were carried out using a CT3001A battery tester (Landt, Vestal, New York, USA) from 0.05 V to 2.5 V. Current densities of 100, 200, 500, and 1000 mA g^{-1} were applied. Cyclic voltammetry experiments were carried out using an IviumStat (Ivium Technologies, Eindhoven, Netherlands).

5 Data availability

The authors confirm that the data supporting the findings of this study are available within the article and its ESI.†

6 Author contributions

K. C. C. performed the experimental work under the supervision of M. B. and I. K. at the University of Manchester and Y. G. at Drexel University, T. Z. synthesized titanium aluminium carbonitride. The analysis was performed by K. C. C. with contributions from all authors. The manuscript was drafted by K. C. C. with input from all authors.

7 Conflicts of interest

The authors declare no conflict of interest.

Acknowledgements

References

1 M. Naguib, et al., Two-dimensional nanocrystals produced by exfoliation of Ti_3AlC_2, Adv. Mater., 2011, 23, 4248–4253.

2 B. Anasori, M. R. Lukatskaya and Y. Gogotsi, 2D metal carbides and nitrides (MXenes) for energy storage, Nat. Rev. Mater., 2017, 2, 16098.

3 R. Ma, et al., Self-Supporting, Binder-Free, and Flexible $Ti_3C_2T_x$ MXene-Based Supercapacitor Electrode with Improved Electrochemical Performance, ACS Nano, 2022, 16, 9713–9727.

4 S. J. Kim, et al., High mass loading, binder-free MXene anodes for high areal capacity Li-ion batteries, Electrochim. Acta, 2015, 163, 246–251.

5 Y. Xie, et al., Prediction and Characterization of MXene Nanosheet Anodes for Non-Lithium-Ion Batteries, ACS Nano, 2014, 8, 9606–9615.

6 M. Naguib, et al., MXene: a promising transition metal carbide anode for lithium-ion batteries, Electrochem. Commun., 2012, 16, 61–64.

7 D. Er, J. Li, M. Naguib, Y. Gogotsi and V. B. Shenoy, Ti_3C_2 MXene as a high capacity electrode material for metal (Li, Na, K, Ca) ion batteries, ACS Appl. Mater. Interfaces, 2014, 6, 11173–11179.

8 F. Shahzad, et al., Electromagnetic interference shielding with 2D transition metal carbides (MXenes), Science, 2016, 353, 1137–1140.

9 A. Iqbal, P. Sambyal and C. M. Koo, 2D MXenes for Electromagnetic Shielding: A Review, Adv. Funct. Mater., 2020, 30, 2000883.

10 J. Lipton, et al., Scalable, Highly Conductive, and Micropatternable MXene Films for Enhanced Electromagnetic Interference Shielding, Matter, 2020, 3, 546–557.

11 Z. W. Seh, et al., Two-Dimensional Molybdenum Carbide (MXene) as an Efficient Electrocatalyst for Hydrogen Evolution, ACS Energy Lett., 2016, 1, 589–594.

12 Y. Gogotsi, The Future of MXenes, Chem. Mater., 2023, 35, 8767–8770.

13 A. Sarycheva and Y. Gogotsi, Raman Spectroscopy Analysis of the Structure and Surface Chemistry of $Ti_3C_2T_x$ MXene, Chem. Mater., 2020, 32, 3480–3488.

14 H. W. Wang, M. Naguib, K. Page, D. J. Wesolowski and Y. Gogotsi, Resolving the Structure of $Ti_3C_2T_x$ MXenes through Multilevel Structural Modeling of the Atomic Pair Distribution Function, Chem. Mater., 2016, 28, 349–359.

15 M. Khazaei, et al., Insights into exfoliation possibility of MAX phases to MXenes, Phys. Chem. Chem. Phys., 2018, 20, 8579–8592.

16 J. Halim, et al., Synthesis and Characterization of 2D Molybdenum Carbide (MXene), Adv. Funct. Mater., 2016, 26, 3118–3127.

17 M. Alhabeb, et al., Selective Etching of Silicon from Ti_3SiC_2 (MAX) to Obtain 2D Titanium Carbide (MXene), Angew. Chem., Int. Ed., 2018, 57, 5444–5448.

18 M. Anayee, et al., Role of acid mixtures etching on the surface chemistry and sodium ion storage in $Ti_3C_2T_x$ MXene, Chem. Commun., 2020, 56, 6090–6093.

19 M. Han, et al., Tailoring electronic and optical properties of MXenes through forming solid solutions, J. Am. Chem. Soc., 2020, 142, 19110–19118.

20 I. Persson, et al., Tailoring Structure, Composition, and Energy Storage Properties of MXenes from Selective Etching of In-Plane, Chemically Ordered MAX Phases, Small, 2018, 14, 1703676.

25174 | J. Mater. Chem. A, 2024, 12, 25165–25175

This journal is © The Royal Society of Chemistry 2024

21 B. Anasori, *et al.*, Control of electronic properties of 2D carbides (MXenes) by manipulating their transition metal layers, *Nanoscale Horiz.*, 2016, **1**, 227–234.

22 M. Naguib, *et al.*, New two-dimensional niobium and vanadium carbides as promising materials for Li-ion batteries, *J. Am. Chem. Soc.*, 2013, **135**, 15966–15969.

23 J.-C. Lei, X. Zhang and Z. Zhou, Recent advances in MXene: preparation, properties, and applications, *Front. Phys.*, 2015, **10**, 107303.

24 M. Alhabeb, *et al.*, Guidelines for Synthesis and Processing of Two-Dimensional Titanium Carbide ($Ti_3C_2T_x$ MXene), *Chem. Mater.*, 2017, **29**, 7633–7644.

25 Y. J. Kim, *et al.*, Etching Mechanism of Monoatomic Aluminum Layers during MXene Synthesis, *Chem. Mater.*, 2021, **33**, 6346–6355.

26 M. Anayee, *et al.*, Kinetics of Ti_3AlC_2 Etching for $Ti_3C_2T_x$ MXene Synthesis, *Chem. Mater.*, 2022, **34**, 9589–9600.

27 A. Gentile, *et al.*, Critical Analysis of MXene Production with *In-Situ* HF Forming Agents for Sustainable Manufacturing, *ChemElectroChem*, 2022, **9**, 202200891.

28 B. Dash, B. R. Das, B. C. Tripathy, I. N. Bhattacharya and S. C. Das, Acid dissolution of alumina from waste aluminium dross, *Hydrometallurgy*, 2008, **92**, 48–53.

29 T. Li, *et al.*, Fluorine-Free Synthesis of High-Purity $Ti_3C_2T_x$ (T=OH, O) *via* Alkali Treatment, *Angew. Chem., Int. Ed.*, 2018, **57**, 6115–6119.

30 C. Peng, *et al.*, A hydrothermal etching route to synthesis of 2D MXene (Ti_3C_2, Nb_2C): enhanced exfoliation and improved adsorption performance, *Ceram. Int.*, 2018, **44**, 18886–18893.

31 H. Dong, *et al.*, Molten Salt Derived Nb_2CT_x MXene Anode for Li-ion Batteries, *ChemElectroChem*, 2021, **8**, 957–962.

32 L. Liu, *et al.*, Exfoliation and Delamination of $Ti_3C_2T_x$ MXene Prepared *via* Molten Salt Etching Route, *ACS Nano*, 2022, **16**, 111–118.

33 M. Li, *et al.*, Element Replacement Approach by Reaction with Lewis Acidic Molten Salts to Synthesize Nanolaminated MAX Phases and MXenes, *J. Am. Chem. Soc.*, 2019, **141**, 4730–4737.

34 R. A. Vaia, *et al.*, Halogen etch of Ti_3AlC_2 MAX phase for MXene fabrication, *ACS Nano*, 2021, **15**, 2771–2777.

35 H. Shi, *et al.*, Ambient-Stable Two-Dimensional Titanium Carbide (MXene) Enabled by Iodine Etching, *Angew. Chem., Int. Ed.*, 2021, **60**, 8689–8693.

36 P. Urbankowski, *et al.*, Synthesis of two-dimensional titanium nitride Ti_4N_3 (MXene), *Nanoscale*, 2016, **8**, 11385–11391.

37 Y. Yang, *et al.*, Electrochemical exfoliation of graphene-like two-dimensional nanomaterials, *Nanoscale*, 2019, **11**, 16–33.

38 A. M. Abdelkader, A. J. Cooper, R. A. W. Dryfe and I. A. Kinloch, How to get between the sheets: a review of recent works on the electrochemical exfoliation of graphene materials from bulk graphite, *Nanoscale*, 2015, **7**, 6944–6956.

39 K. Parvez, *et al.*, Exfoliation of Graphite into Graphene in Aqueous Solutions of Inorganic Salts, *J. Am. Chem. Soc.*, 2014, **136**, 6083–6091.

40 D. C. Marcano, *et al.*, Improved synthesis of graphene oxide, *ACS Nano*, 2010, **4**, 4806–4814.

41 S. Yang, *et al.*, Fluoride-Free Synthesis of Two-Dimensional Titanium Carbide (MXene) Using A Binary Aqueous System, *Angew. Chem.*, 2018, **130**, 15717–15721.

42 S.-Y. Pang, *et al.*, Universal Strategy for HF-Free Facile and Rapid Synthesis of Two-dimensional MXenes as Multifunctional Energy Materials, *J. Am. Chem. Soc.*, 2019, **141**, 9610–9616.

43 M. R. Lukatskaya, *et al.*, Room-Temperature Carbide-Derived Carbon Synthesis by Electrochemical Etching of MAX Phases, *Angew. Chem.*, 2014, **126**, 4977–4980.

44 M. Song, S. Y. Pang, F. Guo, M. C. Wong and J. Hao, Fluoride-Free 2D Niobium Carbide MXenes as Stable and Biocompatible Nanoplatforms for Electrochemical Biosensors with Ultrahigh Sensitivity, *Adv. Sci.*, 2020, **7**, 2001546.

45 W. Sun, *et al.*, Electrochemical etching of Ti_2AlC to Ti_2CT_x (MXene) in low-concentration hydrochloric acid solution, *J. Mater. Chem. A*, 2017, **5**, 21663–21668.

46 J. Chen, *et al.*, Simplified Synthesis of Fluoride-Free $Ti_3C_2T_x$ *via* Electrochemical Etching toward High-Performance Electrochemical Capacitors, *ACS Nano*, 2022, **16**, 2461–2470.

47 M. Shekhirev, C. E. Shuck, A. Sarycheva and Y. Gogotsi, Characterization of MXenes at every step, from their precursors to single flakes and assembled films, *Prog. Mater. Sci.*, 2021, **120**, 100757.

48 S. Célérier, *et al.*, Hydration of $Ti_3C_2T_x$ MXene: An Interstratification Process with Major Implications on Physical Properties, *Chem. Mater.*, 2019, **31**, 454–461.

49 J. Halim, *et al.*, X-ray photoelectron spectroscopy of select multi-layered transition metal carbides (MXenes), *Appl. Surf. Sci.*, 2016, **362**, 406–417.

50 I. Persson, *et al.*, How Much Oxygen Can a MXene Surface Take Before It Breaks?, *Adv. Funct. Mater.*, 2020, **30**, 1909005.

51 V. Augustyn, *et al.*, High-rate electrochemical energy storage through Li^+ intercalation pseudocapacitance, *Nat. Mater.*, 2013, **12**, 518–522.

52 M. R. Lukatskaya, *et al.*, Cation Intercalation and High Volumetric Capacitance of Two-Dimensional Titanium Carbide, *Science*, 2013, **342**, 1502–1506.

53 O. Mashtalir, M. R. Lukatskaya, M. Q. Zhao, M. W. Barsoum and Y. Gogotsi, Amine-assisted delamination of Nb_2C MXene for Li-ion energy storage devices, *Adv. Mater.*, 2015, **27**, 3501–3506.

54 B. Zhang, J. Zhu, P. Shi, W. Wu and F. Wang, Fluoride-free synthesis and microstructure evolution of novel two-dimensional $Ti_3C_2(OH)_2$ nanoribbons as high-performance anode materials for lithium-ion batteries, *Ceram. Int.*, 2019, **45**, 8395–8405.

55 S. Kajiyama, *et al.*, Enhanced Li-Ion Accessibility in MXene Titanium Carbide by Steric Chloride Termination, *Adv. Energy Mater.*, 2017, **7**, 1601873.

56 K. Maleski, C. E. Ren, M. Q. Zhao, B. Anasori and Y. Gogotsi, Size-Dependent Physical and Electrochemical Properties of Two-Dimensional MXene Flakes, *ACS Appl. Mater. Interfaces*, 2018, **10**, 24491–24498.

57 M. Liu, *et al.*, Deformation of and Interfacial Stress Transfer in Ti_3C_2 MXene-Polymer Composites, *ACS Appl. Mater. Interfaces*, 2022, **14**, 10681–10690.

This journal is © The Royal Society of Chemistry 2024

J. Mater. Chem. A, 2024, **12**, 25165–25175 | **25175**